

Intensity Enhanced Cerenkov Luminescence Imaging Using Terbium-Doped Gd_2O_3 Microparticles

Xin Cao,[†] Xueli Chen,[†] Fei Kang,[‡] Yonghua Zhan,[†] Xu Cao,[†] Jing Wang,^{*,‡} Jimin Liang,^{*,†} and Jie Tian^{*,†,§}

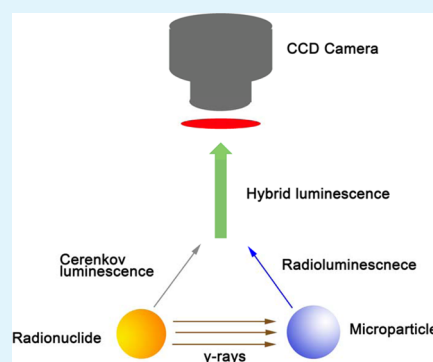
[†]Engineering Research Center of Molecular and Neuro Imaging of the Ministry of Education & School of Life Science and Technology, Xidian University, Xi'an, Shaanxi 710071, China

[‡]Department of Nuclear Medicine, Xijing Hospital, Fourth Military Medical University, Xi'an, Shaanxi 710032, China

[§]Institute of Automation, Chinese Academy of Sciences, Beijing 100190, China

ABSTRACT: Weak intensity and poor penetration depth are two big obstacles toward clinical use of Cerenkov luminescence imaging (CLI). In this proof-of-concept study, we overcame these limitations by using lanthanides-based radioluminescent microparticles (RLMPs), called terbium doped Gd_2O_3 . The characterization experiment showed that the emission excited by Cerenkov luminescence can be neglected whereas the spectrum experiment demonstrated that the RLMPs can actually be excited by γ -rays. A series of in vitro experiments demonstrated that RLMPs significantly improve the intensity and the penetration capacity of CLI, which has been extended to as deep as 15 mm. In vivo pseudotumor study further prove the huge potential of this enhancement strategy for Cerenkov luminescence imaging in living animal studies.

KEYWORDS: biophotonics, imaging, Cerenkov luminescence, radioluminescence, biomaterials



1. INTRODUCTION

Simultaneously providing both functional and molecular information, the dual modality of positron emission tomography (PET) and optical imaging (OI) have some unique and attractive features. For example, they allow concurrent characterization and cross-validation of dual modality imaging probes, provide complementary information on metabolic and protease activity, and improve image quality of the resolution and efficiency.¹ Inspired by this motivation, several groups have been devoted to the development of this technique and its successful application for use in tumor imaging and drug delivery monitoring.^{2–4} Recently developed Cerenkov luminescence imaging (CLI) would provide a perfect solution for dual modality of PET and OI, because both PET and OI can be achieved through a radionuclide probe.⁵ With the advantages of low cost, wide availability, and widely used radionuclides in the clinic, CLI has built a bridge for clinical translation of OI and has become an attractive topic in the field of molecular imaging.^{6–11} In recent years, CLI has been successfully applied in diagnostic imaging (i.e., thyroid and lymph node), therapy monitoring, intraoperative guidance, and endoscopic imaging,^{12–17} applicable to small animals as well as human studies. However, the Cerenkov luminescence (CL) is extremely weak and most of the luminescence is distributed in the spectrum of short wavelengths (below 600 nm).^{4,5,18} Thus, tissue penetration depth of CL is insufficient for the detection of deeply seated targets because of high attenuation of light by biological tissues in ultraviolet or blue wavelengths, which limits

the extensive clinical translations of CLI. To deal with this limitation, one possible solution is to shift the peak wavelength of luminescence light from a short (ultraviolet or blue) to a longer (near-infrared or infrared) one by coupling CL with other fluorescent particles, such as fluorophore,^{19,20} quantum dots,^{7,21–23} and lanthanides.²⁴ In the above scenario, CL is used as excitation source, while the fluorescent particles serve as a fluorescence emitter as in fluorescence imaging. Since near-infrared or infrared light has a lower absorption and less attenuation by tissues than ultraviolet or blue wavelengths, this strategy may be of great significance for the improvement of penetration of CLI.²⁵ However, such an optical-excitation-based enhancement strategy faces two obstacles. First, because of its high absorption in biological tissue, CL is of poor excitation efficiency and can only excite the very nearby fluorescent particles. Second, the redshift of light obeys the law of conservation of energy, so that the intensity of the emitted light is directly dependent on that of CL. If the activity of radionuclides gathered around the target is not sufficient, the red-shifted CL is still unable to detect from a deep lesion. With the properties of emitting visible and near-infrared luminescence under the irradiation of high energy rays, lanthanides-based radioluminescence microparticles (RLMPs) might be

Received: January 15, 2015

Accepted: May 20, 2015

Published: May 20, 2015

promising for solving the limitation of such CL shifting strategy.

Radioluminescence is a phenomenon by which luminescence is produced in materials by bombardment with ionizing radiation of high energy rays, such as X-rays, γ -rays, and beta particles. The materials usually refer to lanthanide-doped particles, such as $\text{Gd}_2\text{O}_2\text{S}:\text{Eu}$, $\text{NaGdF}_4:\text{Eu}_3$, or $\text{Gd}_2\text{O}_2\text{S}:\text{Tb}$.^{26–29}

Because of the relatively high emission efficiency, the RLMPs have been widely used in radiation detectors³⁰ and solid state lighting applications,^{31–34} and they have tremendous potential in the application of biomedical imaging.^{5,29,35} Until now, major applications of RLMPs for biomedical imaging have been focused on studies in which the RLMPs are bombarded with ionizing radiation of X-rays, known as X-ray luminescence tomography (XLT). By this method, X-rays act as an irradiation source, and europium-doped RLMPs (i.e., $\text{Gd}_2\text{O}_2\text{S}:\text{Eu}$ and $\text{NaGdF}_4:\text{Eu}_3$) and terbium (Tb)-doped RLMPs ($\text{Gd}_2\text{O}_2\text{S}:\text{Tb}$) act as a luminescence emitter.^{26,28,35–39} XLT provides a promising solution for the deeply integrated modalities of X-ray computed tomography and optical imaging. According to the principle of XLT, the lanthanides-based RLMPs could also be bombarded by γ -rays that are generated during the decay of radionuclides used in PET, and the produced luminescence could be detected using an optical imaging instrument. This technology is known as radioluminescence imaging (RLI).^{36,40} Compared with the traditional optical-excitation-based enhancement strategy, the tissue absorption of a radioactive excitation source can be ignored since the radioactivity signal of RLI is much more sensitive to detection. The RLI-based enhancement strategy might surpass the weakness and penetration limitation of CLI, facilitating the intensity enhanced CLI technique, and further expand the applications of dual modality of PET and OI.

Hereby, a proof-of-concept study of RLI to enhance the intensity of CLI is presented with a kind of RLMPs, terbium-doped $\text{Gd}_2\text{O}_2\text{S}$ ($\text{Gd}_2\text{O}_2\text{S}:\text{Tb}$). First, characterization of RLMPs was investigated, including scanning electron microscopy (SEM) image, X-ray diffractometer (XRD) pattern, UV–vis–IR absorption spectrum, fluorescence emission spectrum, and γ -rays excited luminescence spectrum. The feasibility and potential of RLMPs-based RLI were then evaluated by a series of in vitro and in vivo pseudotumor experiments. Investigative results revealed that of RLMPs-based RLI is vastly superiority to CLI. Our findings offer an alternative route for enhancing the penetration and intensity of CLI and exploring the possible and potential applications of dual modality of PET and OI.

2. MATERIALS AND METHODS

2.1. Materials. The RLMPs used in this study is terbium-doped $\text{Gd}_2\text{O}_2\text{S}$ ($\text{Gd}_2\text{O}_2\text{S}:\text{Tb}$), which was purchased from Shanghai Keyan Phosphor Technology Co. Ltd. and synthesized using the complex precipitation methods.⁴¹

The radionuclide ^{18}F was obtained in the form of 2–18-fluoro-D-glucose (^{18}F -FDG). ^{18}F -FDG was produced via a cyclotron (GE Industries Inc., USA) and the FDG reagent kit (ABX, Germany).

2.2. Characterization of RLMPs. The RLMPs of $\text{Gd}_2\text{O}_2\text{S}:\text{Tb}$ were characterized by scanning electronic microscopy (SEM), X-ray diffraction (XRD), UV–vis–NIR absorption, and fluorescence emission spectra. A scanning electronic microscope (SEM; S-570, Hitachi, Japan) and an X-ray diffractometer (XRD; Bruker D8 Advance, USA) were utilized to obtain SEM images and XRD patterns; the SEM images provide the size and morphology of RLMPs and the XRD pattern describes its crystal phase. Using a UV–vis–NIR absorption spectrophotometer (UV-2450, Shimadzu, Japan), the absorption

spectrum of RLMPs was measured by flaking them with barium sulfate. On the basis of the measured absorption spectrum, the excited fluorescence emission spectrum of RLMPs was recorded using a fluorescence spectrophotometer (F-4500, Hitachi, Japan). All measurements were performed at room temperature.

To demonstrate whether the RLMPs of $\text{Gd}_2\text{O}_2\text{S}:\text{Tb}$ can emit luminescence by bombardment with the γ -rays emitted from radionuclides, preliminary experiments were conducted. First, an EP tube containing 10 mg of RLMPs was placed into the IVIS system (Caliper Life Science, USA), and then another Epoxy epoxide (EP) tube containing 200 μL of normal saline (NS) was placed at an adjacent position, acting as the control group. Second, the EP tube previously filled with NS in the control group was replaced by another one that contained 7.4 MBq (200 μCi) ^{18}F -FDG with a final volume of 200 μL . Third, the EP tube containing ^{18}F -FDG was covered by a piece of black tape to block the emission of CL. All of the images for the three groups of experiments were acquired with an exposure time of 30 s and replicated 5 times.

2.3. Measurement of Emission Spectrum of RL. The radioactive source containing 5.55 MBq (150 μCi) of ^{18}F -FDG with a final volume of 200 μL was prepared in a single well of a 96-well black plate (Nunc, USA), and an adjacent well was filled with 0.5 mg of RLMPs. The emission spectrum of radioluminescence (RL) emitted from RLMPs excited by γ -rays was measured by the IVIS system equipped with 15 band-pass filters ranging from 500–780 nm, with a 20 nm interval in full width at half-maximum (fwhm). The well containing ^{18}F -FDG was covered by a piece of a black plastic plate.

To investigate the difference between the RLMPs based RL and CL on spectral distribution, the following experiments were conducted. First, 5.55 MBq (150 μCi) of ^{18}F -FDG was thoroughly mixed with 0.5 mg of RLMPs and put into one well of a 96-well black plate. The 96-well black plate was then placed into the field of view (FOV) of the IVIS system to measure the spectrum of RL. Second, a single well of a 96-well black plate was filled with 5.55 MBq (150 μCi) of ^{18}F -FDG and placed into the FOV of the IVIS system to acquire the spectrum of CL.

All of the measurements were acquired with an exposure time of 30 s. The region of interest (ROI) was reasonably extracted from the acquired luminescent image for further analysis, which was applied to all image analysis procedures of the following experiments. The same procedure was repeated 5 times.

2.4. Assessment of Intensity Enhancement of RLI. Two experiments were performed to assay the enhanced intensity of RLI. Samples of ^{18}F -FDG or mixture of ^{18}F -FDG and RLMPs were respectively added into one well of two 96-well black plates. In the first experiment, 3.7 MBq (100 μCi) of ^{18}F -FDG was filled into one well of the first 96-well black plate, and 0.5 mg of RLMPs mixed with 3.7 MBq (100 μCi) of ^{18}F -FDG were added into the other one. The reason for using two 96-well black plates was to avoid the interference of γ -rays from each other. Luminescent images for two samples were detected sequentially using the IVIS system with an exposure time of 30 s. The same procedure was replicated 5 times. The intensity of CLI or RLI was measured by extracting ROIs in luminescent images.

For the second experiment, the radioactivity of ^{18}F -FDG was changed to 1.85 MBq (50 μCi) and the identical procedure was repeated as in the first experiment.

2.5. Relationship between RLI Intensity and the Radioactivity of Radionuclide. 3.7 MBq (100 μCi) of ^{18}F -FDG and 0.5 mg of RLMPs were completely mixed and added into one well of a 96-well black plate with a final volume of 200 μL . After placing the plate in the FOV of IVIS system, white-light and RL images were successively captured. Then the RL images were sequentially acquired for 420 min (about 3.82 half-lives of ^{18}F), with an exposure time of 30 s and acquisition interval of 1 min.

2.6. Relationship between RLI Intensity and the Distance of Radionuclide from RLMPs. In theory, the closer of RLMPs isolated from the radionuclide, the stronger the RL should be. Here, an experiment was performed to investigate the relationship between the RL intensity and distance of radionuclide from RLMPs. In the experiment, 7.4 MBq (200 μCi) ^{18}F -FDG with a volume of 50 μL was

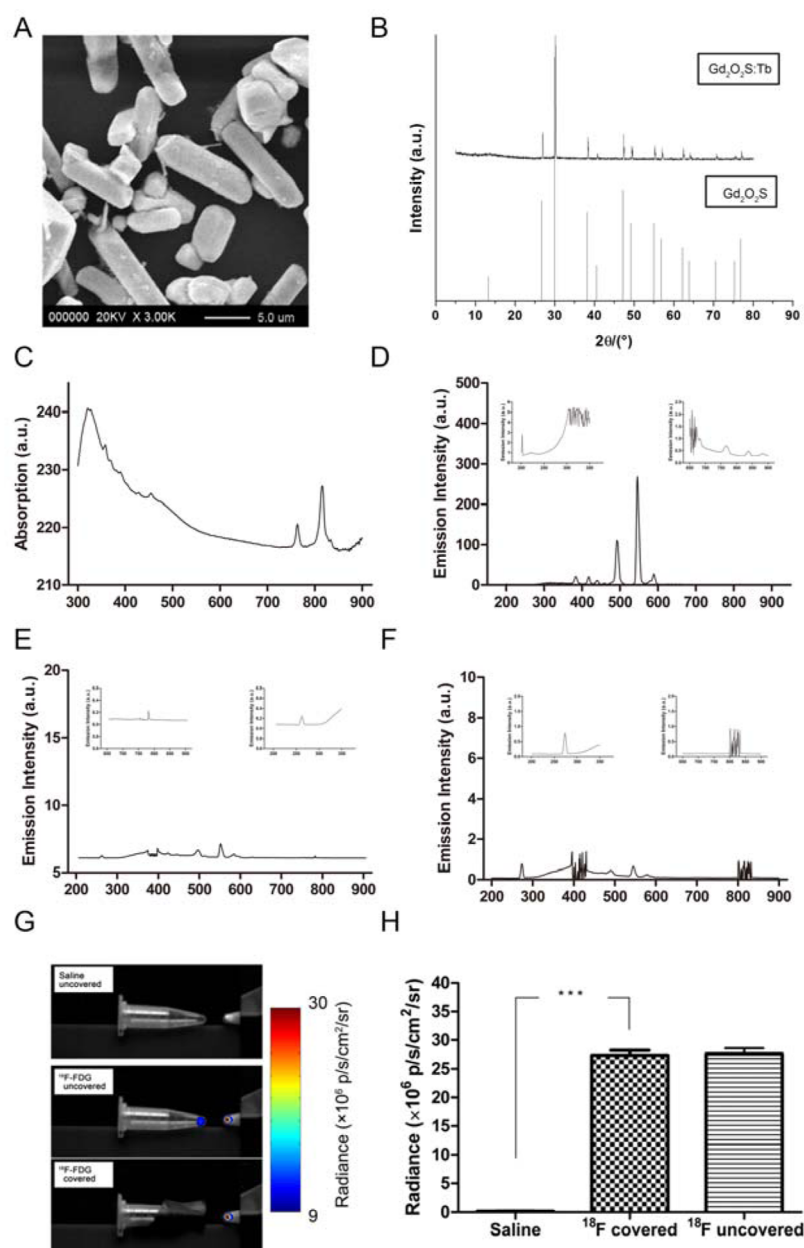


Figure 1. Characterization of RLMPs. (A) SEM image of $\text{Gd}_2\text{O}_2\text{S:Tb}$ particles and (B) XRD pattern of $\text{Gd}_2\text{O}_2\text{S:Tb}$ particles (above), while the bottom is the standard XRD pattern of $\text{Gd}_2\text{O}_2\text{S}$ according to the data of JCPDs card no. 26-1422. (C) UV–vis–NIR absorption spectrum of $\text{Gd}_2\text{O}_2\text{S:Tb}$ particles. (D) Fluorescence emission spectra of $\text{Gd}_2\text{O}_2\text{S:Tb}$ particles under excitation with 321 nm. (E) Fluorescence emission spectra of $\text{Gd}_2\text{O}_2\text{S:Tb}$ particles under excitation with 763 nm; (F) Fluorescence emission spectra of $\text{Gd}_2\text{O}_2\text{S:Tb}$ particles under excitation with 816 nm. (G) Optical images of $\text{Gd}_2\text{O}_2\text{S:Tb}$ under the bombardment of NS, uncovered ^{18}F -FDG, and covered ^{18}F -FDG. (H) Quantitative analysis of panel E, while each ROI is the bottom of EP tube ($P < 0.001$).

added into an EP tube, and 0.5 mg of RLMPs was put into one well of a 96-well black plate. The EP tube was covered with a black tape to prevent the CL emission and then inserted in one well of the plate (only the bottom of EP tube could be inserted into the well). By changing the well where the EP tube was inserted, different distances between the radionuclide and RLMPs could be obtained. For these different distances, RL images were acquired by using the IVIS system with an exposure time of 60 s. The same procedure was once more repeated 5 times.

2.7. Assessment of Penetration Capacity of RLI. Nylon phantom-based experiments were conducted to investigate the penetration capacity of RLI. Six cubic phantoms were manufactured and a hole was drilled into each one from its upper surface. Distance from the center of the holes to the side surface varied from 0–15 mm

(0, 2.5, 5, 7.5, 10, and 15 mm), which produced a series of investigation depths. A rubber capillary tube filled with a mixture of 3.7 MBq (100 μCi) ^{18}F -FDG and 0.5 mg RLMPs was inserted into the hole of a phantom. The phantom was then placed in the FOV of the IVIS system and a luminescent image was obtained. In addition, to demonstrate the superiority of RLI over CLI in penetration capacity, another rubber capillary tube was filled only with 3.7 MBq (100 μCi) of ^{18}F -FDG and inserted into the hole of each phantom to repeat the above experiment. All of the luminescent images were collected with an exposure time of 30 s and the same procedure was replicated 5 times.

2.8. Pseudotumor Assessment of RLI. To investigate the potential of RLI for biomedical applications, pseudotumor based experiments were performed in this section. Two subcutaneous

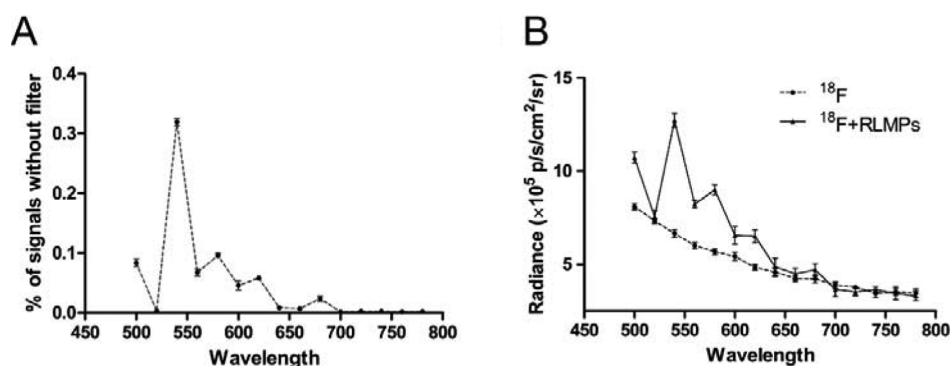


Figure 2. Emission spectra of RLNPs. (A) Emission spectrum of RL from $\text{Gd}_2\text{O}_2\text{S:Tb}$ excited by γ -rays. (B) Emission spectra of luminescence from a mixture of ^{18}F -FDG and $\text{Gd}_2\text{O}_2\text{S:Tb}$ (solid line), as well as a mixture of ^{18}F -FDG and NS (dotted line).

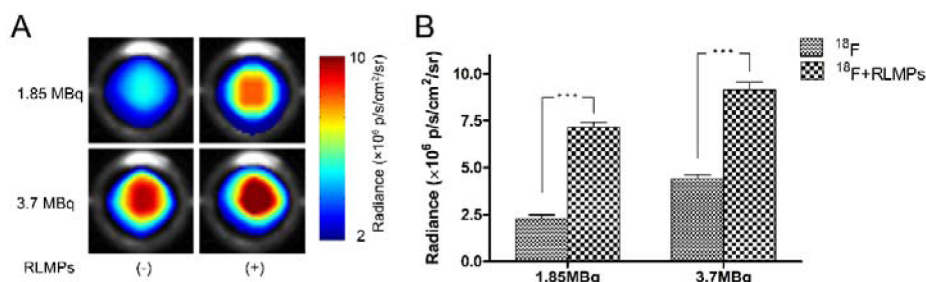


Figure 3. Assessment of intensity enhancement of RLI. (A) Fusion images for different activities of ^{18}F -FDG mixed with or without RLMPs. (B) Quantitative analysis of panel A (***) $P < 0.006$.

pseudotumors were deposited on either side of the back of several living mice ($n = 5$), according to previous studies.^{17,42} All of the following animal procedures were performed under general anesthesia by inhalation of a 1%–2% isoflurane-oxygen mixture. Then 3.7 MBq (100 μCi) ^{18}F -FDG was mixed with 40 μL of Matrigel (BD Biosciences, USA) and NS to form a final mixture with a volume of 150 μL . This is known as the Matrigel + ^{18}F -FDG mixture, which was subcutaneously injected in the left flank of all the mice. On the right flank, a mixture with a volume of 150 μL , in which 3.7 MBq (100 μCi) ^{18}F -FDG, 0.5 mg RLMPs, and 40 μL Matrigel were thoroughly mixed (Matrigel + RLMPs + ^{18}F -FDG mixture) was implanted subcutaneously. The mice were kept warm for 5 min until the Matrigel was solidified, and were then scanned with the micro-PET/CT system (Mediso Ltd., Hungary). After finishing the PET/CT scans, the mice were transferred into the IVIS system and optical images were acquired with an exposure time of 1 min. Radiance of each pseudotumor was calculated by extracting ROIs in luminescent images and the relevant radioactivity was calculated based on PET/CT imaging using the 3D-ROI method. For quantitative analysis, optical radiance was normalized by the radioactivity in the same pseudotumor.

All of the animal care and protocols were approved by the Fourth Military Medical University Animal Studies Committee (Protocol 20090260).

3. RESULTS

3.1. Characterization of RLMPs. One of the representative SEM images of $\text{Gd}_2\text{O}_2\text{S:Tb}$ is shown in Figure 1A. The SEM image shows a rod-like structure of synthesized crystals, with the granularity of 2–8 μm . Although the size of the synthesized crystals figures in the micron scale, they can also be synthesized into nanoparticles with a suitable synthetic method.³⁷ XRD patterns of $\text{Gd}_2\text{O}_2\text{S:Tb}$ are presented in Figure 1B and the host is shown as a hexagonal phase of $\text{Gd}_2\text{O}_2\text{S}$ according to the data of JCPDS card no. 26-1422, which agrees well with the published results.³⁷ The UV–vis–NIR spectrum of $\text{Gd}_2\text{O}_2\text{S:Tb}$, as shown in Figure 1C, exhibits characteristic

absorption peaks at 321, 763, and 816 nm. Using the absorption peak wavelengths as the excitation source, respectively, the corresponding emission spectra of $\text{Gd}_2\text{O}_2\text{S:Tb}$ are illustrated in Figure 1D and F. As can be seen, there is no fluorescence emission under the irradiation of 763 and 816 nm excitation source. For the excitation source of 321 nm, two obvious peaks can be observed at 546 and 493 nm. However, compared with the intensity of the excitation source, excitation efficiency is too low for imaging studies, with a value being less than 2%.

Figure 1G shows images of $\text{Gd}_2\text{O}_2\text{S:Tb}$ under the bombardment of NS, uncovered ^{18}F -FDG, and covered ^{18}F -FDG, while Figure 1H presents a quantitative analysis of 1G. From Figures 1G and 1H, the following conclusions can be stated. First, there is no luminescence emission for $\text{Gd}_2\text{O}_2\text{S:Tb}$ itself in the surrounding environment. Second, the $\text{Gd}_2\text{O}_2\text{S:Tb}$ can actually be excited by γ -rays emitted from ^{18}F -FDG for both the uncovered and covered groups, and the intensity of emitted RL is much higher than that of CL emitted from uncovered ^{18}F -FDG. Third, intensities of RL emitted from $\text{Gd}_2\text{O}_2\text{S:Tb}$ are nearly equal for both the uncovered and covered groups, with the ratio of intensity from covered to uncovered group being 0.989, revealing that the luminescence emission from $\text{Gd}_2\text{O}_2\text{S:Tb}$ is mainly excited by γ -rays. Although the $\text{Gd}_2\text{O}_2\text{S:Tb}$ may also be excited by CL, as seen in the fluorescence absorption and emission spectrum of Figures 1C–1F, the ratio is so low that its contribution can be ignored.

3.2. Measurement of Emission Spectrum of RL. The emission spectrum of RL from $\text{Gd}_2\text{O}_2\text{S:Tb}$ excited by γ -rays from isolated radionuclides is shown in Figure 2A, which depicts the same peak wavelength (around 540 nm) as that excited by X-rays.³⁷ Figure 2B presents the emission spectra of luminescence from mixture of ^{18}F -FDG and $\text{Gd}_2\text{O}_2\text{S:Tb}$ (solid line), as well as a mixture of ^{18}F -FDG and NS (dotted line). A

similar spectral distribution is obtained between $\text{Gd}_2\text{O}_2\text{S:Tb}$ mixed with ^{18}F -FDG and isolated from one another, with the same peaks located around 540 nm. As expected, the intensity of Cerenkov luminescence (CL) emitted from a mixture of ^{18}F -FDG and NS is obviously increased with the help of utilizing $\text{Gd}_2\text{O}_2\text{S:Tb}$.

3.3. Assessment of Intensity Enhancement of RLI.

Fusion images of luminescence and white light are shown in Figure 3A. The left column shows images of CL from a mixture of ^{18}F -FDG and NS (^{18}F -FDG + NS), and the right column presents images of luminescence from mixture of ^{18}F -FDG and $\text{Gd}_2\text{O}_2\text{S:Tb}$ (^{18}F -FDG + $\text{Gd}_2\text{O}_2\text{S:Tb}$). The first row contains results obtained using 1.85 MBq (50 μCi) ^{18}F -FDG, and the second row depicts those using 3.7 MBq (100 μCi) ^{18}F -FDG. Figure 3B reveals the quantitative analysis of Figure 3A. Results of Figure 3A intuitively illustrate that luminescence intensity is enhanced for ^{18}F -FDG + $\text{Gd}_2\text{O}_2\text{S:Tb}$ compared with CL from ^{18}F -FDG + NS. When radioactivity of the radionuclide is 3.7 MBq (100 μCi), the ratio of emission radiance of ^{18}F -FDG + $\text{Gd}_2\text{O}_2\text{S:Tb}$ to that of ^{18}F -FDG + NS is about 3.12. As the measured luminescence of ^{18}F -FDG + $\text{Gd}_2\text{O}_2\text{S:Tb}$ contains two parts, the CL from the radionuclide itself and RL from RLMPs excited by γ -rays, the enhancement ratio does not remain unchanged. Regarding the CL intensity of ^{18}F -FDG + NS in two groups of experiments, it could suggest that 1.85 MBq (50 μCi) ^{18}F -FDG has emitted sufficient γ -rays to excite 0.5 mg of RLMPs, so that the increase of radioactivity (3.7 MBq (100 μCi)) cannot excite the RLMPs to emit more luminescence. Thus, the increased intensity of luminescence for the ^{18}F -FDG + $\text{Gd}_2\text{O}_2\text{S:Tb}$ groups should be induced by the increase of CL emitted from the extra radionuclide. This is because the increased value of intensity for the ^{18}F -FDG + $\text{Gd}_2\text{O}_2\text{S:Tb}$ groups is equal to that of CL, with the value about $2.116\,000\text{ p s}^{-1}\text{ cm}^{-2}\text{ sr}^{-1}$.

3.4. Relationship between RLI Intensity and the Radioactivity of Radionuclide. Figure 4 shows the variation

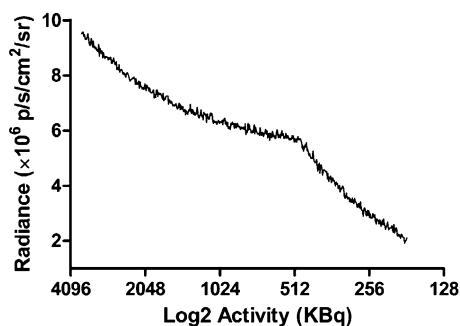


Figure 4. Variation of luminescence intensity emitted from mixture of ^{18}F -FDG and RLMPs with the decay of ^{18}F -FDG.

of luminescence intensity emitted from a mixture of ^{18}F -FDG and RLMPs with the decay of ^{18}F -FDG. From Figure 4, it is easily observed that the declining trend of luminescence intensity has exacerbated the demarcation point of 474.34 KBq (12.82 μCi), corresponding to the time period of 326 min. Using this demarcation point, the measurements are divided into two groups, the measured data before 326 min and those after 326 min. A linear regression model was used to fit the two groups of measurements and calculate the slope of their fitting curves, respectively. For the group before 326 min, the slope is about $-1192\text{ p s}^{-1}\text{ cm}^{-2}\text{ sr}^{-1}\text{ KBq}^{-1}$ with $R^2 = 0.9923$; while for

the group after 326 min, the slope has exacerbated to $-11360\text{ p s}^{-1}\text{ cm}^{-2}\text{ sr}^{-1}\text{ KBq}^{-1}$ ($R^2 = 0.9893$). From the results of last subsection, the descending slope for CL was calculated, with the value about $-1144.17\text{ p s}^{-1}\text{ cm}^{-2}\text{ sr}^{-1}\text{ KBq}^{-1}$, which is almost the same as that in the group before 326 min. Thus, interesting conclusions can be drawn that the decline of luminescence intensity mainly results from the decrease of CL before the decay time of 326 min and the sharper decrease of luminescence intensity after the decay time of 326 min is induced by the combined decrease of CL from radionuclides and RL from RLMPs. This indicates that there is a saturation radioactivity of ^{18}F -FDG for exciting 0.5 mg RLMPs, being about 474.34 KBq (12.82 μCi).

3.5. Relationship between RLI Intensity and the Distance of Radionuclide from RLMPs. Photograph of the experimental design is shown in Figure 5A, where spatial relationships between the radionuclide and RLMPs can be clearly observed. Because the size of one well of a 96-well black plate is 7 mm in diameter, the minimum distance scale is set to be 7 mm. Figure 5B presents the fusion images of RL and white light for different distances, which intuitively exhibits the attenuation of RL intensity with the increase of distance. Figure 5C depicts the quantitative analysis of Figure 5B. Using a curve-fitting method, a nonlinear relationship between RLI intensity and the distance of the radionuclide from RLMPs is obtained with $R^2 = 0.9901$ and $P < 10^{-5}$, expressing an exponential attenuation of RLI intensity with the increase of distance, which is in accordance with theoretical calculation.

3.6. Assessment of Penetration Capacity of RLI. Fusion images of luminescence and white light for different depths are shown in Figure 6A. The first row presents results of the ^{18}F -FDG + RLMPs group, and the second row corresponds to those of ^{18}F -FDG + NS. It is obvious that the intensity of CLI from ^{18}F -FDG + NS attenuates faster than that of RLI from ^{18}F -FDG + RLMPs with increasing depth. Figure 6B presents a quantitative analysis of Figure 6A, from which it can be seen that even at a depth of 15 mm, the radiance of RLI from ^{18}F -FDG + RLMPs is twice that of CLI from ^{18}F -FDG + NS.

3.7. In Vivo Assessment of RLI. Figure 7A shows the result of the micro-PET/CT scans, which reveals that the radioactivity of ^{18}F -FDG was nearly the same in both pseudotumors. However, an obvious difference is observed for optical images, as shown in Figure 7B. Much brighter signals are achieved in the pseudotumor on the right flanks of mice, which can be quantitatively assessed in Figure 7C. Quantitative analysis in Figure 7C illustrates that the intensity of RL from the pseudotumor containing ^{18}F -FDG mixed with RLMPs is significant greater than that of CL from the contralateral pseudotumor that contains the solution of ^{18}F -FDG with NS (153.2 ± 25.54 vs 422.6 ± 57.03 ; $n = 5$, $p < 0.001$)

4. DISCUSSION

During the transference of CLI technology to clinic applications, the weak intensity and poor penetration depth represent two big obstacles. In this proof-of-concept study, an emerging radioluminescence imaging (RLI) technique is demonstrated to overcome these limitations by using lanthanides-based radioluminescent microparticles (RLMPs) called terbium-doped $\text{Gd}_2\text{O}_2\text{S}$. With a series of in vitro and in vivo pseudotumor experiments, we show that RLMPs-based RLI significantly improves the intensity and penetration capacity of CLI, facilitating the intensity enhanced CLI technique using the terbium-doped $\text{Gd}_2\text{O}_2\text{S}$ microparticles.

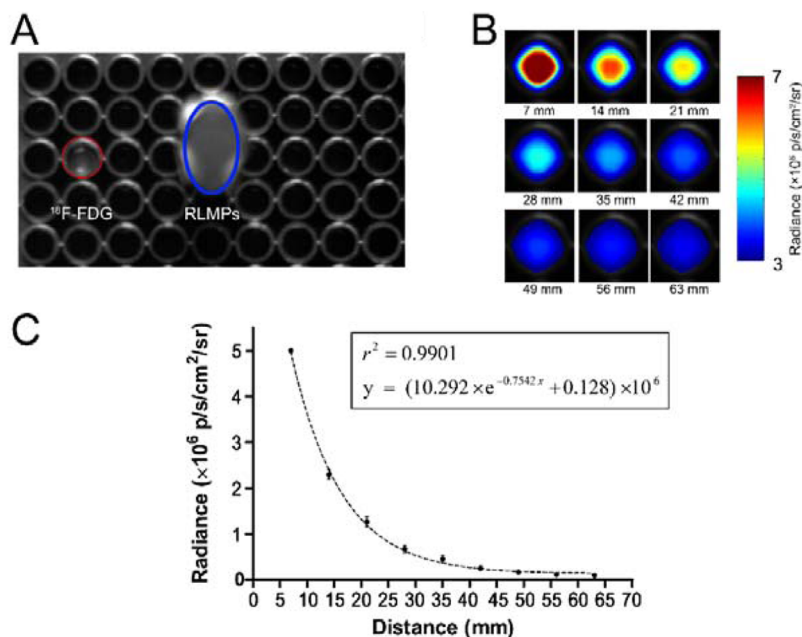


Figure 5. Results of the relationship between RLI intensity and the distance of radionuclide from RLMPs. (A) Photograph of the 96-well black plate, the red circle indicates the well containing 0.5 mg of RLMPs, while the blue one illustrates the EP tube containing 7.4 MBq (200 μ Ci) 18 F-FDG. (B) Fusion images of RL and white-light ones for different distances, including 7, 14, 21, 28, 35, 42, 49, 56, and 63 mm, respectively. (C) Quantitative analysis of panel B.

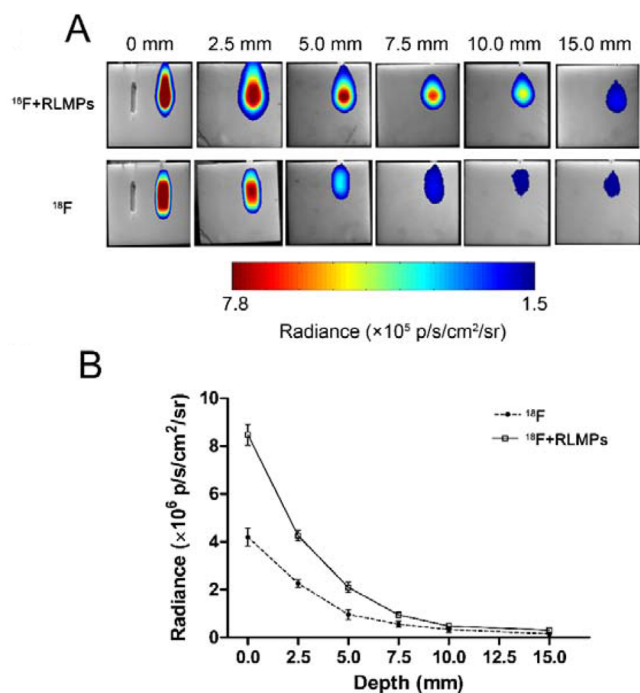


Figure 6. Results of penetration capacity of RLI. (A) Fusion images for different depths, including 0, 2.5, 5, 7.5, 10, 12.5, and 15 mm. (B) Quantitative analysis of panel A.

In all of the experiments, the radionuclide used is 18 F-FDG, one kind of β^+ radionuclides that produces γ -rays and is widely used in clinics for PET scanning. First, results of the characterization and emission-spectrum-measurement experiments reveal that the $\text{Gd}_2\text{O}_2\text{S}:\text{Tb}$ -based RLMPs can be excited by γ -rays, but can hardly be excited by Cerenkov luminescence (CL). Peak wavelength of emission spectra excited by γ -rays is around 540 nm, which is consistent with that excited by X-

rays.³⁷ Although the $\text{Gd}_2\text{O}_2\text{S}:\text{Tb}$ -based RLMPs can emit fluorescence under the irradiation of 321 nm ultraviolet light (Figure 1C–1F), the ratio of luminescence excited by CL is so low that its contribution can be neglected (about 1.1%). However, as the shape of RLMPs can affect the emission efficiency under the irradiation of UV, with a more suitable shape, the ratio may increase a bit.⁴³ Second, compared with CL emitted from a solution of 18 F-FDG and NS, the intensity of RL emitted from a mixture of 18 F-FDG and RLMPs can be significantly enhanced, with a 3.12-fold enhancement at radioactivity of 1.85 MBq (50 μ Ci), demonstrating the superiority of RLI over CLI in intensity. Furthermore, the maximum saturation dose for 18 F-FDG exciting RLMPs was investigated and calculated as 474.34 KBq (12.82 μ Ci) per 0.5 mg RLMPs, indicating that the enhancement ratio is not a constant. For a fixed amount of RLMPs, the lower the activity of 18 F-FDG (it must be larger than the maximum saturation dose), the larger the enhancement ratio will be obtained. Third, the distance evaluation experiment shows that the RL intensity has an exponential relationship with the distance between radioactive sources and RLMPs, indicating that the RLMPs can be superbly excited by the surrounding radionuclides. Fourthly, in a penetration assessment experiment, much better penetration capacity was obtained for RLI than CLI with the help of RLMPs. Even at depth of 15 mm, the penetration intensity of RLI is as twice that of CLI. Lastly, the feasibility of RLI technique in application of in vivo studies is validated with pseudotumor experiments, whose results demonstrated that the RLMPs-based RLI technique has a great potential in the in vivo biomedical applications. Compared with traditional CLI, the RLMPs-based RLI exhibits a much better penetration capacity with much brighter signals.

Because most of the radionuclides have been widely used in clinical diagnosis and treatment, CLI has been recognized as a potential optical imaging modality for clinical translation. However, the weak intensity and poor penetration capacity of

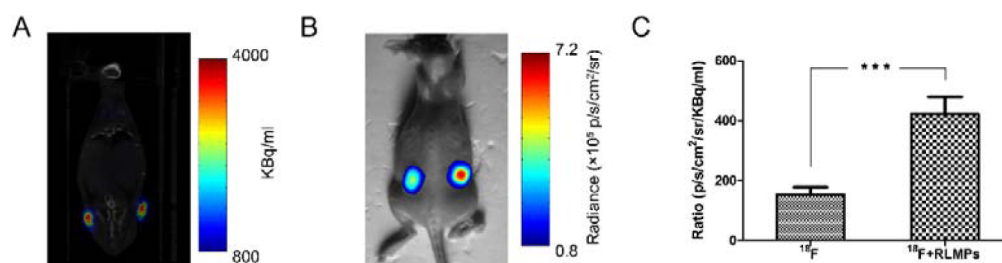


Figure 7. Results of the pseudotumor model based animal experiment. (A) Image of Micro-PET/CT scan. (B) Fusion image of subcutaneous pseudotumor. (C) Quantitative analysis of panel B (***) ($P < 0.001$).

CLI prohibits its in vivo application, especially for clinical application. The RLMPs-based RLI technique might overcome the limitations of CLI in clinical applications. Referring to the aspect of the translational potential, although the RLMPs had not been employed as a probe until now, the probe made by this material could be seen as a great potential tool for clinical translation of optical imaging. First, according to our results, the RL signal presents a sharply negative correlation to the excitation distance, which is roughly consistent with the relationship between the radioactive exposure rate and distance. Thus, the characteristics of this material guarantees an intense excitation effect specifically from nearby excitation sources, ensuring both the sensitivity and specificity of the RLMPs-based probe in the future. Second, cytotoxicity of the probe is another obstacle for optical imaging translating to clinic. However, the biological safety of the lanthanides-based material has been well established.^{44,45}

Although the feasibility and potential of RLI has been well demonstrated with one kind of lanthanides-based RLMPs, terbium-doped Gd_2O_2S ($Gd_2O_2S:Tb$), some problems remain unsolved. First, in this proof-of-concept study, the lanthanides-based RLMPs in this paper have not been made as a targeted probe so that they cannot be directly used in biological/ biomedical applications. Second, the lanthanides-based RLMPs selected in this proof-of-concept study is $Gd_2O_2S:Tb$. Even though it can emit somewhat stronger luminescence than CL with the intensive part of the spectrum located in the range of 520–550 nm, it is still not the optimal spectrum for biological optical imaging. Because in biological optical imaging, the near-infrared light ranging from 600–900 nm has a relatively lower absorption and less attenuation in tissues.^{18,25} Our future work will focus on the synthesis of new RL materials with longer emission wavelengths, the modification of RL materials to nanoscale, and the functionalization of cancer specificity.

5. CONCLUSION

In conclusion, the feasibility and potential of RLMPs-based RLI technique was explored in this study, which overcame the weakness and penetration limitations of CLI, facilitating the intensity enhanced CLI technique, and providing a new path for the development of dual modality PET-OI technology. Investigation results indicate the great potential of RLMPs-based RLI technique in applications of clinical setting.

AUTHOR INFORMATION

Corresponding Authors

*E-mail: wangjing@fmmu.edu.cn.

*E-mail: jimleung@mail.xidian.edu.cn.

*E-mail: tian@ieee.org.

Author Contributions

Xin Cao, Xueli Chen, and Fei Kang contributed equally.

Funding

This work was partly supported by the Program of National Basic Research and Development Program of China (973) under Grant No. 2011CB707702, the National Natural Science Foundation of China under Grant Nos. 81090272, 81227901, 81101083, 81230033, 61405149, 81401442, the Natural Science Basic Research Plan in Shaanxi Province of China under Grant No. 2015JQ6249 and 2015JZ019, and the Fundamental Research Funds for the Central Universities.

Notes

The authors declare no competing financial interest.

ACKNOWLEDGMENTS

This work was partly supported by the Program of National Basic Research and Development Program of China (973) under Grant No. 2011CB707702, the National Natural Science Foundation of China under Grant Nos. 81090272, 81227901, 81101083, 81230033, 61405149, and 81401442, the Natural Science Basic Research Plan in Shaanxi Province of China under Grant No. 2015JQ6249 and 2015JZ019, and the Fundamental Research Funds for the Central Universities.

REFERENCES

- (1) Li, C. Q.; Yang, Y. F.; Mitchell, G. S.; Cherry, S. R. Simultaneous PET and multispectral 3-dimensional fluorescence optical tomography imaging system. *J. Nucl. Med.* **2011**, *52*, 1268–1275.
- (2) Pandey, S. K.; Kaur, J.; Easwaramoorthy, B.; Shah, A.; Coleman, R.; Mukherjee, J. Multimodality imaging probe for positron emission tomography and fluorescence imaging studies. *Mol. Imaging* **2014**, *13*, 1–7.
- (3) Zhang, Y.; Hong, H.; Engle, J. W.; Yang, Y.; Theuer, C. P.; Barnhart, T. E.; Cai, W. Positron emission tomography and optical imaging of tumor CD105 expression with a dual-labeled monoclonal antibody. *Mol. Pharmaceutics* **2012**, *9*, 645–653.
- (4) Nahrendorf, M.; Kelihir, E.; Marinelli, B.; Waterman, P.; Feruglio, P. F.; Fexon, L.; Pivovarov, M.; Swirski, F. K.; Pittet, M. J.; Vinegoni, C.; Weissleder, R. Hybrid PET–optical imaging using targeted probes. *Proc. Natl. Acad. Sci. U. S. A.* **2010**, *107*, 7910–7915.
- (5) Robertson, R.; Germanos, M. S.; Li, C.; Mitchell, G. S.; Cherry, S. R.; Silva, M. D. Optical imaging of Cerenkov light generation from positron-emitting radiotracers. *Phys. Med. Biol.* **2009**, *54*, N355–N365.
- (6) Xu, Y.; Chang, E.; Liu, H.; Jiang, H.; Gambhir, S. S.; Cheng, Z. Proof-of-concept study of monitoring cancer drug therapy with cerenkov luminescence imaging. *J. Nucl. Med.* **2012**, *53*, 312–317.
- (7) Liu, H. G.; Ren, G.; Miao, Z.; Zhang, X. F.; Tang, X. D.; Han, P. Z.; Gambhir, S. S.; Cheng, Z. Molecular optical imaging with radioactive probes. *PLoS One* **2010**, *5*, No. e9470.
- (8) Robertson, R.; Germanos, M. S.; Manfredi, M. G.; Smith, P. G.; Silva, M. D. Multimodal imaging with ^{18}F -FDG PET and Cerenkov

luminescence imaging after MLN4924 treatment in a human lymphoma xenograft model. *J. Nucl. Med.* **2011**, *52*, 1764–1769.

(9) Ruggiero, A.; Holland, J. P.; Lewis, J. S.; Grimm, J. Cerenkov luminescence imaging of medical isotopes. *J. Nucl. Med.* **2010**, *51*, 1123–1130.

(10) Thorek, D. L. J.; Das, S.; Grimm, J. Molecular imaging using nanoparticle quenchers of Cerenkov luminescence. *Small* **2014**, *10*, 3729–3734.

(11) Jeong, S. Y.; Hwang, M. H.; Kim, J. E.; Kang, S.; Park, J. C.; Yoo, J.; Ha, J. H.; Lee, S. W.; Ahn, B. C.; Lee, J. Combined Cerenkov luminescence and nuclear imaging of radioiodine in the thyroid gland and thyroid cancer cells expressing sodium iodide symporter: Initial feasibility study. *Endocr. J.* **2011**, *58*, 575–583.

(12) Spinelli, A. E.; Ferdeghini, M.; Cavedon, C.; Zivelonghi, E.; Calandrino, R.; Fenzi, A.; Sbarbati, A.; Boschi, F. First human cerenkography. *J. Biomed. Opt.* **2013**, *18*, No. 020502.

(13) Balkin, E. R.; Kenoyer, A.; Orozco, J. J.; Hernandez, A.; Shadman, M.; Fisher, D. R.; Green, D. J.; Hylarides, M. D.; Press, O. W.; Wilbur, D. S.; Pagel, J. M. In Vivo Localization of ^{90}Y and ^{177}Lu Radioimmunoconjugates Using Cerenkov Luminescence Imaging in a Disseminated Murine Leukemia Model. *Cancer Res.* **2014**, *74*, 5846–54.

(14) Madru, R.; Tran, T. A.; Axelsson, J.; Ingvar, C.; Bibic, A.; Ståhlberg, F.; Knutsson, L.; Strand, S.-E. ^{68}Ga -labeled superparamagnetic iron oxide nanoparticles (SPIONs) for multi-modality PET/MR/Cerenkov luminescence imaging of sentinel lymph nodes. *Am. J. Nucl. Med. Mol. Imaging* **2014**, *4*, 60–69.

(15) Thorek, D. L.; Riedl, C.; Grimm, J. Clinical Cerenkov luminescence imaging of ^{18}F -FDG. *J. Nucl. Med.* **2014**, *55* (1), 95–98 DOI: 10.2967/jnumed.113.127266.

(16) Liu, H.; Carpenter, C. M.; Jiang, H.; Pratz, G.; Sun, C.; Buchin, M. P.; Gambhir, S. S.; Xing, L.; Cheng, Z. Intraoperative imaging of tumors using Cerenkov luminescence endoscopy: a feasibility experimental study. *J. Nucl. Med.* **2012**, *53*, 1579–1584.

(17) Cao, X.; Chen, X.; Kang, F.; Lin, Y.; Liu, M.; Hu, H.; Nie, Y.; Wu, K.; Wang, J.; Liang, J. Performance evaluation of endoscopic Cerenkov luminescence imaging system: in vitro and pseudotumor studies. *Biomed. Opt. Express* **2014**, *5*, 3660–3670.

(18) Xu, Y.; Liu, H.; Cheng, Z. Harnessing the power of radionuclides for optical imaging: Cerenkov luminescence imaging. *J. Nucl. Med.* **2011**, *52*, 2009–2018.

(19) Lewis, M. A.; Kodibagkar, V. D.; Öz, O. K.; Mason, R. P. On the potential for molecular imaging with Cerenkov luminescence. *Opt. Lett.* **2010**, *35*, 3889–3891.

(20) Bernhard, Y.; Collin, B.; Decreau, R. A. Inter/intramolecular Cerenkov radiation energy transfer (CRET) from a fluorophore with a built-in radionuclide. *Chem. Commun. (Camb.)* **2014**, *50*, 6711–6713.

(21) Dothager, R. S.; Goiffon, R. J.; Jackson, E.; Harpstrite, S.; Piwnica-Worms, D. Cerenkov radiation energy transfer (CRET) imaging: A novel method for optical imaging of PET isotopes in biological systems. *PLoS One* **2010**, *5*, No. e13300.

(22) Kotagiri, N.; Niedzwiedzki, D. M.; Ohara, K.; Achilefu, S. Activatable probes based on distance-dependent luminescence associated with Cerenkov radiation. *Angew. Chem., Int. Ed.* **2013**, *52*, 7756–7760.

(23) Thorek, D. L.; Ogirala, A.; Beattie, B. J.; Grimm, J. Quantitative imaging of disease signatures through radioactive decay signal conversion. *Nat. Med.* **2013**, *19*, 1345–1350.

(24) Ma, X.; Kang, F.; Xu, F.; Feng, A.; Zhao, Y.; Lu, T.; Yang, W.; Wang, Z.; Lin, M.; Wang, J. Enhancement of Cerenkov luminescence imaging by dual excitation of Er^{3+} , Yb^{3+} -doped rare-earth micro-particles. *PLoS One* **2013**, *8*, No. e77926.

(25) Smith, A. M.; Mancini, M. C.; Nie, S. Bioimaging: Second window for in vivo imaging. *Nat. Nanotechnol.* **2009**, *4*, 710–711.

(26) Sun, C.; Pratz, G.; Carpenter, C. M.; Liu, H.; Cheng, Z.; Gambhir, S. S.; Xing, L. Synthesis and radioluminescence of PEGylated Eu^{3+} -doped nanophosphors as bioimaging probes. *Adv. Mater.* **2011**, *23*, H195–H199.

(27) Liu, X.; Liao, Q.; Wang, H. Fast X-ray luminescence computed tomography imaging. *IEEE Trans. Biomed. Eng.* **2014**, *61*, 1621–1627.

(28) Sudheendra, L.; Das, G. K.; Li, C.; Stark, D.; Cena, J.; Cherry, S.; Kennedy, I. M. $\text{NaGdF}_4: \text{Eu}^{3+}$ nanoparticles for enhanced X-ray excited optical imaging. *Chem. Mater.* **2014**, *26*, 1881–1888.

(29) Chen, H.; Longfield, D. E.; Varahagiri, V. S.; Nguyen, K. T.; Patrick, A. L.; Qian, H.; VanDerveer, D. G.; Anker, J. N. Optical imaging in tissue with X-ray excited luminescent sensors. *Analyst* **2011**, *136*, 3438–3445.

(30) Shen, J.; Sun, L. D.; Yan, C. H. Luminescent rare earth nanomaterials for bioprobe applications. *Dalton Trans.* **2008**, 5687–5697.

(31) Kumar, V.; Som, S.; Kumar, V.; Kumar, V.; Ntwaeaborwa, O.; Coetsee, E.; Swart, H. Tunable and white emission from ZnO: Tb^{3+} nanophosphors for solid state lighting applications. *Chem. Eng. J.* **2014**, *255*, 541–552.

(32) Som, S.; Kunti, A.; Kumar, V.; Kumar, V.; Dutta, S.; Chowdhury, M.; Sharma, S.; Terblans, J.; Swart, H. Defect correlated fluorescent quenching and electron phonon coupling in the spectral transition of Eu^{3+} in CaTiO_3 for red emission in display application. *J. Appl. Phys.* **2014**, *115*, No. 193101.

(33) Kumar, V.; Bedyal, A.; Sharma, J.; Kumar, V.; Ntwaeaborwa, O.; Swart, H. Spectral and surface investigations of $\text{Ca}_2\text{V}_2\text{O}_7: \text{Eu}^{3+}$ nanophosphors prepared by citrate-gel combustion method: A potential red-emitting phosphor for near-UV light-emitting diodes. *Appl. Phys. A: Mater. Sci. Process.* **2014**, *116*, 1785–1792.

(34) Som, S.; Mitra, P.; Kumar, V.; Kumar, V.; Terblans, J.; Swart, H.; Sharma, S. The energy transfer phenomena and colour tunability in $\text{Y}_2\text{O}_3\text{: Eu}^{3+}/\text{Dy}^{3+}$ micro-fibers for white emission in solid state lighting applications. *Dalton Trans.* **2014**, *43*, 9860–9871.

(35) Carpenter, C.; Sun, C.; Pratz, G.; Rao, R.; Xing, L. Hybrid X-ray/optical luminescence imaging: Characterization of experimental conditions. *Med. Phys.* **2010**, *37*, 4011–4018.

(36) Carpenter, C. M.; Sun, C.; Pratz, G.; Liu, H.; Cheng, Z.; Xing, L. Radioluminescent nanophosphors enable multiplexed small-animal imaging. *Opt. Express* **2012**, *20*, 11598–11604.

(37) Chen, H.; Moore, T.; Qi, B.; Colvin, D. C.; Jelen, E. K.; Hitchcock, D. A.; He, J.; Mefford, O. T.; Gore, J. C.; Alexis, F. Monitoring pH-triggered drug release from radioluminescent nanocapsules with X-ray excited optical luminescence. *ACS Nano* **2013**, *7*, 1178–1187.

(38) Chen, D.; Zhu, S.; Yi, H.; Zhang, X.; Chen, D.; Liang, J.; Tian, J. Cone beam X-ray luminescence computed tomography: A feasibility study. *Med. Phys.* **2013**, *40*, No. 031111.

(39) Chen, D.; Zhu, S.; Chen, X.; Chao, T.; Cao, X.; Zhao, F.; Huang, L.; Liang, J. Quantitative cone beam X-ray luminescence tomography/X-ray computed tomography imaging. *Appl. Phys. Lett.* **2014**, *105*, No. 191104.

(40) Sun, C.; Pratz, G.; Carpenter, C. M.; Liu, H.; Cheng, Z.; Gambhir, S. S.; Xing, L. Synthesis and radioluminescence of PEGylated Eu^{3+} -doped nanophosphors as bioimaging probes. *Adv. Mater.* **2011**, *23*, H195–H199.

(41) Tian, Y.; Cao, W.-H.; Luo, X.-X.; Fu, Y. Preparation and luminescence property of $\text{Gd}_2\text{O}_3\text{: Tb}$ X-ray nano-phosphors using the complex precipitation method. *J. Alloys Compd.* **2007**, *433*, 313–317.

(42) Liu, H. G.; Zhang, X. F.; Xing, B. G.; Han, P. Z.; Gambhir, S. S.; Cheng, Z. Radiation-luminescence-excited quantum dots for in vivo multiplexed optical imaging. *Small* **2010**, *6*, 1087–1091.

(43) Xu, L.; Shen, J.; Lu, C.; Chen, Y.; Hou, W. Self-assembled three-dimensional architectures of $\text{Y}_2(\text{WO}_4)_3: \text{Eu}$: Controlled synthesis, growth mechanism, and shape-dependent luminescence properties. *Cryst. Growth Des.* **2009**, *9*, 3129–3136.

(44) Chatterjee, D. K.; Rufaihah, A. J.; Zhang, Y. Upconversion fluorescence imaging of cells and small animals using lanthanide doped nanocrystals. *Biomaterials* **2008**, *29*, 937–943.

(45) Xiong, L.; Yang, T.; Yang, Y.; Xu, C.; Li, F. Long-term in vivo biodistribution imaging and toxicity of polyacrylic acid-coated upconversion nanophosphors. *Biomaterials* **2010**, *31*, 7078–7085.